



Structure effect of graphene on the photocatalytic performance of plasmonic Ag/Ag₂CO₃-rGO for photocatalytic elimination of pollutants

Shaoqing Song ^{a,b}, Bei Cheng ^a, Nanshi Wu ^a, Aiyun Meng ^a, Shaowen Cao ^a, Jiaguo Yu ^{a,c,*}

^a State Key Laboratory of Advanced Technology for Material Synthesis and Processing, Wuhan University of Technology, Wuhan 430070, People's Republic of China

^b Key Laboratory of Radioactive Geology and Exploration Technology Fundamental Science for National Defense, School of Chemistry, Biology and Material, East China Institute of Technology, Nanchang, Jiangxi Province 330013, PR China

^c Faculty of Science, King Abdulaziz University, Jeddah 21589, Saudi Arabia



ARTICLE INFO

Article history:

Received 22 April 2015

Received in revised form 18 July 2015

Accepted 20 July 2015

Available online 29 July 2015

Keywords:

Graphene

Structure effect

Plasmonic Ag

Ag₂CO₃

Photocatalysis

ABSTRACT

Introducing plasmonic metal onto semiconductor materials has been proven to be an attractive strategy for enhancing the photocatalytic activity in the visible region by tuning the morphologies, sizes and compositions of plasmonic metal to form the strong surface plasmon resonance. Here we utilized the structure effect of reduced graphene oxide (rGO) to construct highly efficient plasmonic photocatalysts for the photocatalytic oxidation of pollutants. Plasmonic Ag/Ag₂CO₃-rGO was facilely prepared by the spontaneous redox of Ag⁺ and the defect structures of rGO. Characterization and photocatalytic tests showed that defect structures of rGO promoted the formation of plasmonic Ag, and graphitic structures reduced the recombination rate of photogenerated electrons and holes. Thus, the as-constructed Ag/Ag₂CO₃-rGO photocatalysts exhibited a much higher photocatalytic activity than the Ag₂CO₃ and Ag₂CO₃-GO-1.0 composite in the photocatalytic oxidation of organic pollutant, and the Ag/Ag₂CO₃-rGO (1.0 wt% rGO) showed the optimum photocatalytic performance. This work may lead to a new strategy for exploring the advanced photocatalysts of semiconductors and rGO composite by utilizing the structures of rGO for the photocatalytic elimination of pollutants.

© 2015 Elsevier B.V. All rights reserved.

1. Introduction

Photocatalytic technology has attracted much attention for the direct application of solar energy in environmental cleaning, organic synthesis, and energy producing [1–5]. Although conventional TiO₂ possesses excellent photocatalytic activity and stability, it can only function under UV light (ca. 4% of the solar spectrum). Therefore, it is highly desirable to develop novel photocatalysts that can directly utilize visible light from sunlight. In general, there are some strategies to explore highly efficient photocatalysts. First, doping metallic/nonmetallic elements (Fe, V, and Cr or N, S, and C) into TiO₂ and BiOCl [6–16]; second, exploring semiconductor materials with small band gap energies, such as CdS, CuS, Bi₂WO₆, Bi₂O₃, Fe₂O₃, Bi₂O₃, Cu₂O and silver-containing compounds (Ag₃PO₄, AgGaO₂, Ag₃VO₄, and Ag₂CO₃) [17–37]. However, these strategies still show constraints including low photocatalytic efficiency, poor stability, and limited visible-light absorption. As a

potential alternative, introducing plasmonic Au or Ag nanoparticles (NPs) onto semiconductor materials have been shown to effectively enhance the photocatalytic activity in the visible region due to the strong surface plasmon resonance (SPR) [38–43]. For example, plasmonic Ag NPs on Ag₃PO₄ and AgCl can promote the photocatalytic efficiency and enhance the stability of these Ag-based photocatalysts [30,40]. Study results indicate that the SPR intensity is dependent on the metal species, the sizes and shapes. Thus, researchers focus on the preparation of semiconductor-based plasmonic photocatalysts to precisely control the shapes and sizes of the metal NPs [44–46]. Actually, the structural and electronic properties of semiconductor materials can also be facilely improved by the appropriate cocatalysts or supports.

Owing to high electron mobility, high surface area, and high transparency, graphene including graphene oxide (GO) and reduced graphene oxide (rGO), a unique sp² hybrid carbon network material, has been used as an ideal cocatalyst or support to improve the photocatalytic efficiency [2,3,47]. Various GO/semiconductor composite photocatalysts have been prepared, e.g., GO/TiO₂ [48], graphene/CdS [49–52], GO/Ag/AgX (X = Cl, Br) [53–55], and GO/Ag₃PO₄ [56,57]. Generally, GO or rGO prepared

* Corresponding author. Fax: +86 27 87879468.

E-mail address: jiaguoyu@yahoo.com (J. Yu).

by chemical methods is composed of graphitic, oxygen-containing groups and defects (S1 in Supplementary Materials). Studies show that the electronic properties of graphene materials are related to the structures of graphene. The oxygen bonds on graphene lead to the valence band changes from the π -orbital of graphene to the O 2p orbital, which thus will result in a larger bandgap [58,59]. Moreover, defects of sp^2 carbon materials show the reducibility and can reduce some of metal ions spontaneously [60]. Thus, graphene with suitable structures can regulate the structural and electronic properties of metal NPs (e.g., Ag, Pt or Au) instead of the tedious and complicated chemical synthesis. Inspired by this, the plasmonic Ag supported on the composite photocatalysts of Ag_2CO_3 and reduced graphene oxide (Ag/Ag_2CO_3 -rGO) was facilely designed through utilizing the structure properties of graphene in this study. We systematically studied the effect of the structures of rGO on the SPR of Ag and the photocatalytic performance of Ag/Ag_2CO_3 -rGO. The results showed that the defect structures of rGO played an important role in the design of plasmonic Ag/Ag_2CO_3 -rGO composite photocatalysts. Moreover, graphitic structures of rGO with efficient electron-transfer ability reduced the recombination of photogenerated electrons and holes via the rapid transfer of photogenerated electrons from the photocatalytic materials to rGO. Thus, the as-constructed Ag/Ag_2CO_3 -rGO photocatalysts presented high catalytic activity and stability for the photocatalytic oxidation decomposition of methyl orange (MO) and phenol.

2. Experimental

2.1. Preparation of rGO and Ag/Ag_2CO_3 -rGO

GO was synthesized by the modified Hummers' method. In short, 1 g of nature graphite (325 mesh, Alfa Aesar) was added to 92 mL of concentrated sulfuric acid under stir and ice-water bath for 1 h. Then 6 g of potassium permanganate was slowly added, and the mixture was stirred at 20 °C for 1 h. Next, 92 mL of distilled water was added, and the mixture was further stirred for 30 min with increasing the temperature to 90 °C. Finally, 280 mL of distilled water and 20 mL of H_2O_2 (30%) were dropwise added, and the color of the solution changed from dark brown to yellow. The obtained GO was separated by centrifugation, washed with deionized (DI) water, and finally dried under vacuum. And the obtained GO (100 mg) was dispersed into 100 mL of DI water by sonication for 0.5 h, and then 0.2 g of $NaBH_4$ was added into the GO solution and magnetically stirred for 0.5 h. The mixture was then refluxed at 80 °C for 5 h and washed 4 times with DI water. After filtration, the obtained sample was dried in vacuum oven at 70 °C and labeled as rGO. rGO was impregnated into 50 mL of $AgNO_3$ (0.058 M) aqueous solution under stirring followed by ultrasonic treatment for 25 min to ensure the adsorption of positively charged Ag^+ onto the surface of negatively charged rGO via electrostatic interaction [61]. Then 50 mL of $NaHCO_3$ (0.029 M) was added with drop by drop to the above solution, and the precipitates would be formed. The obtained samples were washed with water to remove the residual ions and dried in a vacuum at 60 °C for 1 h. According to the dosage of rGO in the samples, the three samples with rGO were synthesized and denoted as Ag/Ag_2CO_3 -rGO-0.5, Ag/Ag_2CO_3 -rGO-1.0 and Ag/Ag_2CO_3 -rGO-1.5 corresponding to the mass content of rGO of 0.5%, 1.0% and 1.5%. All the preparation procedures were proceeded in beaker covered with tinfoil. For comparison, pristine Ag_2CO_3 and Ag_2CO_3 -GO-1.0 were prepared according to the similar procedure but without rGO or with the addition of 1.0% of GO. The obtained Ag_2CO_3 and Ag_2CO_3 -GO-1.0 were further irradiated with visible-light for 45 min. And Ag NPs were formed on Ag_2CO_3 or Ag_2CO_3 -GO-1.0, and these two photocatalysts were denoted as Ag/Ag_2CO_3 -vis or Ag/Ag_2CO_3 -GO-vis. Nitrogen doped

TiO_2 ($TiO_{1.98}N_{0.02}$: N-TiO₂) photocatalyst was prepared according to the reported method [62].

2.2. Characterization

Morphological analysis was taken by using a field-emission scanning electron microscope (SEM, Hitachi, Japan). The X-ray diffraction (XRD) measurements were performed on a Rigaku RINT-2000 instrument with using $Cu K\alpha$ radiation (40 kv) from 10° to 90° at a scanning rate of 0.067°/s. UV/vis absorption spectra were taken at room temperature on a UV-2550 (Shimadzu) spectrometer. X-ray photoelectron spectroscopy (XPS) measurements were done on a VG ESCALAB 210 XPS spectrometer system with $Mg K\alpha$ source. All the binding energies were referenced to the C1s peak at 284.8 eV of the surface adventitious carbon. Cyclic voltammetry (CV) tests were performed at 25 °C in a three-electrode cell connected to a CHI 660C workstation (CH Instrument, Inc.). The working electrode was a glassy carbon disk with an area of 0.071 cm². $Ag/AgCl$ and platinum wire served as reference and auxiliary electrodes, respectively. Thin film electrode for rGO was prepared by the following procedure. Simply, the rGO suspension with a concentration of 1.0 mg mL⁻¹ was obtained with the aid of ultrasonic dispersion, and 20 μ L of suspension was dropped onto the glassy carbon disk. After evaporating the solvent under an infrared heat lamp, 0.5 μ L of Nafion (Dupont, 5 wt%) was dropped onto rGO film to act as binder. The redox potential of rGO was examined by the CV tests which were obtained in B-R buffer solution at a scanning rate of 50 mV s⁻¹.

2.3. Photocatalytic tests

The photocatalytic activity tests of the prepared samples were evaluated by the photocatalytic decomposition removal of MO and phenol solutions at ambient temperature. In the catalytic process, 0.05 g of the sample was dispersed and then suffered an adsorption–desorption equilibrium in 25 mL of MO solution (10 mg/L) or phenol (10 mg/L). Afterwards, a 350W xenon lamp equipped with a cutoff filter of 420 nm was used as a visible-light source, and the average light intensity was about 40 mW/cm². The concentration of MO (or phenol) was analyzed by an UV–visible spectrophotometer (UV-1240, SHIMADZU, Japan). After visible-light irradiation, a certain amount of solution mixture was centrifuged to identify the concentration change of MO (or phenol) at set intervals.

3. Results and discussion

3.1. Composition and morphology of the catalysts

Fig. 1 displays XRD patterns of the as-prepared Ag_2CO_3 based samples. The peaks at 26.1° (marked with #) for the samples arise from the (0 0 2) plane of graphite in GO or rGO (lines b–e), while the ones at 18.61°, 20.66°, 32.76°, 33.76°, 37.09°, 39.75°, 41.91° and 44.45° result from the (0 2 0), (1 1 0), (−1 0 1), (−1 3 0), (2 0 0), (0 3 1), (2 2 0) and (1 3 1) diffractions of the monoclinic phase Ag_2CO_3 (JCPDS card No. 70-2184) (lines a–e). Moreover, a slow scan was operated to detect the influence of rGO and/or GO on the composition and phase of Ag_2CO_3 . It is seen that a gradually enhanced diffraction peak appears at 38.3° along with increasing the content of rGO (lines c–e of inset in **Fig. 1**). This peak corresponds to the (1 1 1) plane of the metallic Ag phase [29,30,38], suggesting the formation of a small amount of metallic Ag along with the generation of Ag_2CO_3 after the addition of rGO. However, this metal Ag phase was not found in the cases for the Ag_2CO_3 as well as Ag_2CO_3 -GO-1.0 samples (lines a and b).

The chemical states and the surface composition of the samples have been analyzed by XPS (**Fig. 2**). Ag 3d spectra present

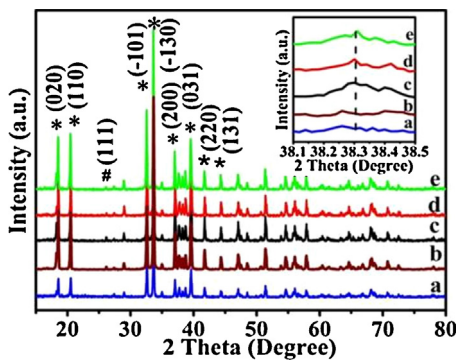


Fig. 1. XRD patterns for Ag_2CO_3 and $\text{Ag}/\text{Ag}_2\text{CO}_3$ -rGO samples: (a) Ag_2CO_3 , (b) Ag_2CO_3 -GO-1.0, (c) $\text{Ag}/\text{Ag}_2\text{CO}_3$ -rGO-0.5, (d) $\text{Ag}/\text{Ag}_2\text{CO}_3$ -rGO-1.0 and (e) $\text{Ag}/\text{Ag}_2\text{CO}_3$ -rGO-1.5.

two main peaks located at ~ 367.7 and 373.7 eV, corresponding to $\text{Ag 3d}_{5/2}$ and $\text{Ag 3d}_{3/2}$ [63]. The width at half maximum broadens from 1.23, 1.29, 1.38 to 1.50 eV and the asymmetry becomes obvious accompanied with increasing the rGO content from 0, 0.5, 1.0 to 1.5% (Fig. 2A). The Ag 3d signals of $\text{Ag}/\text{Ag}_2\text{CO}_3$ -rGO can be deconvoluted into two components centered at 367.7/373.7 and 368.2/374.2 eV, ascribed to the characteristics of Ag^+ and metal Ag, respectively (Table 1). Quantitative analysis on the surface Ag/Ag^+ molar ratios is 0.11, 0.13 and 0.35 corresponding to $\text{Ag}/\text{Ag}_2\text{CO}_3$ -rGO-0.5, $\text{Ag}/\text{Ag}_2\text{CO}_3$ -rGO-1.0 and $\text{Ag}/\text{Ag}_2\text{CO}_3$ -rGO-1.5 (Fig. 2B and Table 1). This produced Ag phase was clearly observed in SEM images for $\text{Ag}/\text{Ag}_2\text{CO}_3$ -rGO samples (Fig. 3). It is seen that Ag_2CO_3 in pure Ag_2CO_3 and Ag_2CO_3 -GO-1.0 samples are irregular cuboids with a length from 1 to 3 μm , and the cuboid surface is very smooth (Fig. 3A and F). After the participation of rGO, the unique NPs appear and disperse evenly on the surface of Ag_2CO_3 , and the size decreases greatly from ~ 50 nm to ~ 20 nm but the density increases gradually (Fig. 3B–E). Combined with the results of XRD and XPS, it can be confirmed that Ag NPs were introduced on Ag_2CO_3 after the addition of rGO. Obviously, the rGO plays an important role in the size and content of Ag in $\text{Ag}/\text{Ag}_2\text{CO}_3$ -rGO samples.

3.2. The formation mechanism of $\text{Ag}/\text{Ag}_2\text{CO}_3$ -rGO

In the absence of reductant or photo-assistance, the formation of Ag NPs on the surface of Ag_2CO_3 is attributed to the spontaneous redox reaction between rGO and Ag^+ . And the driving force for the redox process is the positive ΔE between the reduction potential of Ag^+ ($\varphi_{\text{Ag}^+/\text{Ag}}$) and the oxidation potential of rGO ($\varphi_{\text{R-rGO/O-rGO}}$) [60]:

$$\Delta E = \varphi_{\text{Ag}^+/\text{Ag}} - \varphi_{\text{R-rGO/O-rGO}} > 0 \quad (\text{A.1})$$

It is known that

$$\varphi_{\text{Ag}^+/\text{Ag}} \approx 0.7996 + 0.059 \log([\text{Ag}^+]/[\text{Ag}]) \quad (\text{A.2})$$

The concentration of Ag^+ ($[\text{Ag}^+]$) is 0.058 M, and thus $\varphi_{\text{Ag}^+/\text{Ag}}$ is 0.63 V in the presented reaction system. The redox potentials of rGO were studied by CV in B-R buffer solution with pH from 1.9 to 11.0 considering the pH variation before and after the addition of NaHCO_3 , as presented in Fig. 4. It is seen that a pair of broad redox peaks appears in each CV curve obtained in the electrolyte with different pH values, which correlates with the oxidation and reduction of defects in rGO. In detail, with increasing the pH value of the electrolyte, the oxidation potential of the defects negatively shifts from 0.28 to 0.26, 0.11 and -0.01 V vs. Ag/AgCl electrode, which corresponds to a potential of 0.477, 0.457, 0.307 and 0.187 V vs. SHE electrode. Hence, the driving force of ΔE for the spontaneous redox reaction between Ag^+ and rGO is 0.153, 0.173, 0.323

and 0.443 V according to Eq. (1). Therefore, the condition for spontaneous reduction of Ag^+ to Ag on rGO is satisfied thermodynamically during each step of preparation from the addition of AgNO_3 to the participation of NaHCO_3 . Based on the above experimental results and analysis, the synthesis mechanism of $\text{Ag}/\text{Ag}_2\text{CO}_3$ -rGO is proposed and illustrated in Fig. 5. The reaction involves three stages: (1) The absorption of Ag^+ ions to rGO; (2) The spontaneous reduction of Ag^+ ions and the oxidation of the defects in rGO occur due to the positive ΔE between the two half reactions, and the formed Ag NPs on rGO or even between rGO sheets have been clearly observed by SEM (Fig. S2A and B in Supplementary material); (3) After the addition of NaHCO_3 , the negatively shifted oxidation potential of defects in rGO ensures the proceeding of the spontaneous reaction and part Ag NPs will suspend in the solution apart from on the rGO. At the same time, the Ag^+ ions were precipitated in the form of Ag_2CO_3 cuboids and the suspended Ag NPs can be adsorbed on the surface of Ag_2CO_3 cuboids and also on rGO.

The structural changes of GO and rGO before and after the spontaneous reduction of Ag^+ should be traced due to the important role of rGO on the preparation of $\text{Ag}/\text{Ag}_2\text{CO}_3$ -rGO, which have been revealed by Raman spectroscopy (Fig. 6). It is seen that, the rGO shows a higher I_D/I_G ratio (1.10, line b) than GO (0.85, line a), indicating the reduction of oxygen-containing groups in GO by NaBH_4 and more defects existing in rGO. It should be noted that the value of I_D/I_G for the rGO in $\text{Ag}/\text{Ag}_2\text{CO}_3$ -rGO-1.0 is 1.02. This value is lower than that of 1.10 in pure rGO because of the re-oxidation of the defects to oxygen-containing groups by the redox reaction with Ag^+ ions [60], while it is higher than the value of 0.85 in GO, indicating parts of defects in rGO were well maintained after the spontaneous redox reaction.

3.3. Optical absorption properties of photocatalysts

The optical absorption properties of Ag_2CO_3 and $\text{Ag}/\text{Ag}_2\text{CO}_3$ -rGO samples were studied by UV-vis diffuse reflectance spectra (Fig. 7) since the optical absorption behavior of a photocatalyst was essential for its photocatalytic activity. All the $\text{Ag}/\text{Ag}_2\text{CO}_3$ -rGO samples display similar absorption edge with an intense transition from the visible to UV region, implying that Ag and graphene do not incorporate into the lattice of Ag_2CO_3 or influence its bandgap width. With increasing amount of the rGO, the $\text{Ag}/\text{Ag}_2\text{CO}_3$ -rGO composites show a continuously enhanced visible-light absorption in the range of 400–800 nm, which is attributed to the grafting of rGO and the SPR effect of Ag on $\text{Ag}/\text{Ag}_2\text{CO}_3$ -rGO. Especially, the SPR absorption of Ag is mainly located in the region of 480–550 nm, which favors visible light absorption and the corresponding photocatalytic performance of $\text{Ag}/\text{Ag}_2\text{CO}_3$ -rGO [38].

3.4. Photocatalytic activity and stability under visible-light

The photocatalytic performance of $\text{Ag}/\text{Ag}_2\text{CO}_3$ -rGO composites was investigated firstly by photocatalytic oxidation of MO. MO solution without photocatalysts was irradiated under visible-light for 80 min, and the concentration shows no obvious decrease, indicating that MO molecule is relatively stable and the self-photolysis process can be ignored (Fig. S3 in Supplementary Materials). The photocatalytic oxidation of MO was completed in 50 min with Ag_2CO_3 as a photocatalyst, and the completed reaction time decreases to 30, 15 and 25 min over $\text{Ag}/\text{Ag}_2\text{CO}_3$ -rGO-0.5, $\text{Ag}/\text{Ag}_2\text{CO}_3$ -rGO-1.0, and $\text{Ag}/\text{Ag}_2\text{CO}_3$ -rGO-1.5, respectively (Fig. 8A). The apparent rate constant (k) was calculated on the basis of pseudo first order kinetics, as shown in Fig. 8C and Table 2. It is clear that the $\text{Ag}/\text{Ag}_2\text{CO}_3$ -rGO catalysts show much higher k values than Ag_2CO_3 . Particularly, the k for the optimized $\text{Ag}/\text{Ag}_2\text{CO}_3$ -rGO-1.0 sample is 0.18 min^{-1} , which is 3.6 times higher than that for Ag_2CO_3 (0.05 min^{-1}). And the results indicate that rGO as cocat-

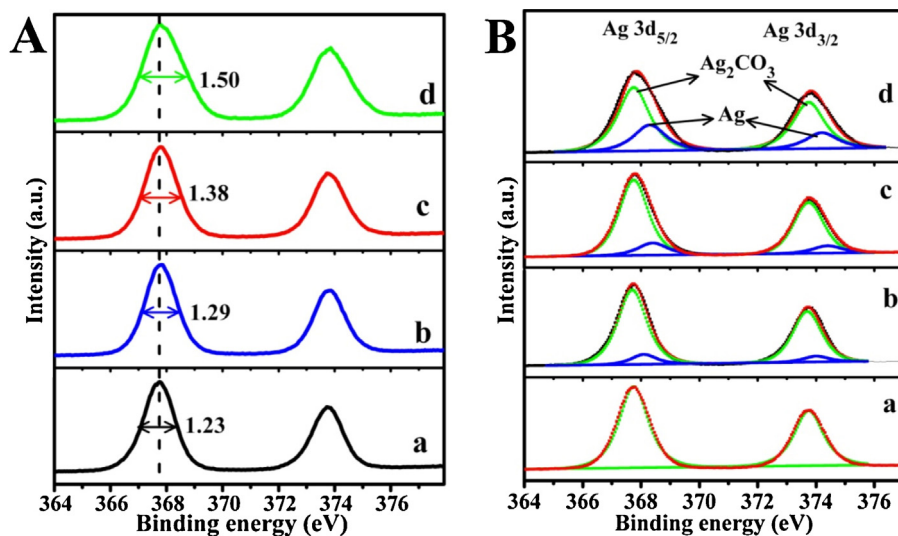


Fig. 2. XPS profiles for Ag_2CO_3 and $\text{Ag}/\text{Ag}_2\text{CO}_3$ -rGO samples. (a) Ag_2CO_3 , (b) $\text{Ag}/\text{Ag}_2\text{CO}_3$ -rGO-0.5, (c) $\text{Ag}/\text{Ag}_2\text{CO}_3$ -rGO-1.0 and (d) $\text{Ag}/\text{Ag}_2\text{CO}_3$ -rGO-1.5.

Table 1

The deconvoluted XPS peaks from the $\text{Ag } 3\text{d}_{5/2}$ signals in the prepared photocatalysts.

Samples	Peak positions (eV)	FWHM (eV)	Area (a.u.)	Peak area ratio
$\text{Ag}/\text{Ag}_2\text{CO}_3$ -rGO-0.5	368.25/367.71	1.16/1.15	3528/32073	0.11
$\text{Ag}/\text{Ag}_2\text{CO}_3$ -rGO-1.0	368.20/367.74	1.19/1.20	3278/25215	0.13
$\text{Ag}/\text{Ag}_2\text{CO}_3$ -rGO-1.5	368.20/367.73	1.23/1.22	4842/14241	0.34
$\text{Ag}/\text{Ag}_2\text{CO}_3$ -GO-vis	368.28/367.70	1.18/1.21	2562/19708	0.13
Ag_2CO_3	367.82	1.23	24311	/

alyst can promote the photocatalytic activities of Ag_2CO_3 based photocatalysts.

To further investigate the influence of rGO and Ag NPs or SPR effect on the photocatalytic performance, $\text{Ag}/\text{Ag}_2\text{CO}_3$ -vis, Ag_2CO_3 -GO-1.0, $\text{Ag}/\text{Ag}_2\text{CO}_3$ -GO-vis and N-TiO_2 were used as the photocatalyst in the photocatalytic decomposition removal of MO

(Fig. 8B). In Fig. 8B, N-TiO_2 employed as photocatalyst shows the lowest activity among these photocatalysts, suggesting that photocatalysts based on Ag_2CO_3 are the more efficient visible-light photocatalysts. Moreover, it is seen the rate constants for MO degradation over Ag_2CO_3 -based photocatalyst were improved from 0.05 (Ag_2CO_3) to 0.08 ($\text{Ag}/\text{Ag}_2\text{CO}_3$ -vis) and from 0.07 (Ag_2CO_3 -GO-1.0)

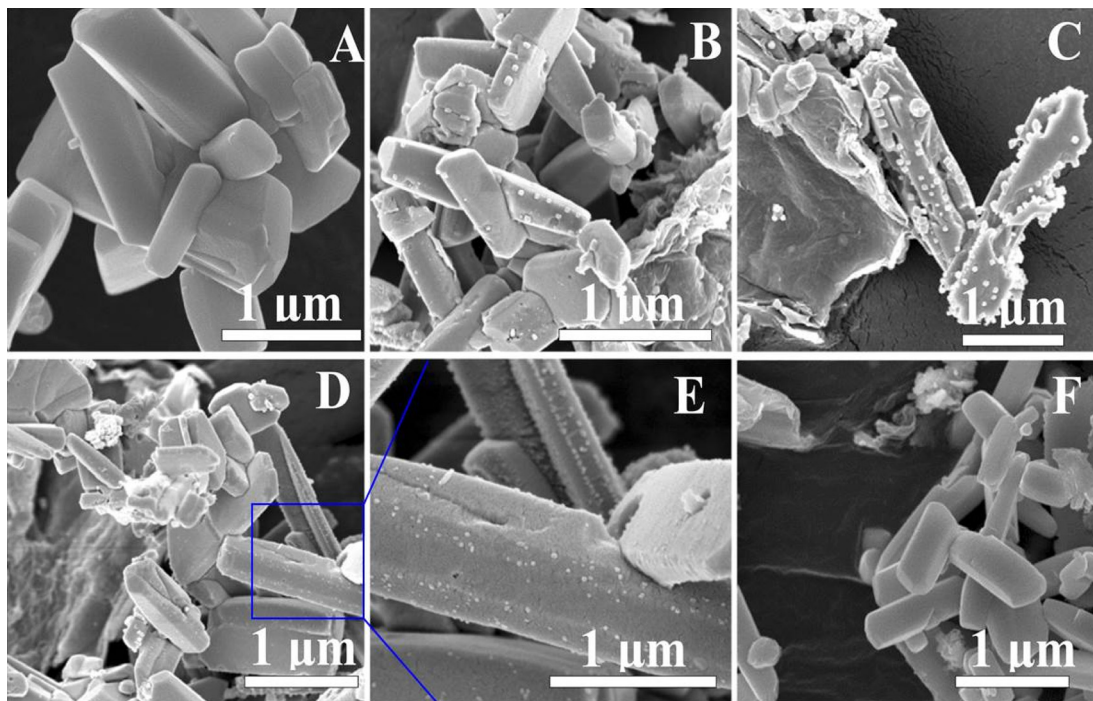


Fig. 3. SEM images of Ag_2CO_3 and $\text{Ag}/\text{Ag}_2\text{CO}_3$ -rGO. (A) Ag_2CO_3 , (B) $\text{Ag}/\text{Ag}_2\text{CO}_3$ -rGO-0.5, (C) $\text{Ag}/\text{Ag}_2\text{CO}_3$ -rGO-1.0, (D, E) $\text{Ag}/\text{Ag}_2\text{CO}_3$ -rGO-1.5, and (F) Ag_2CO_3 -GO-1.0.

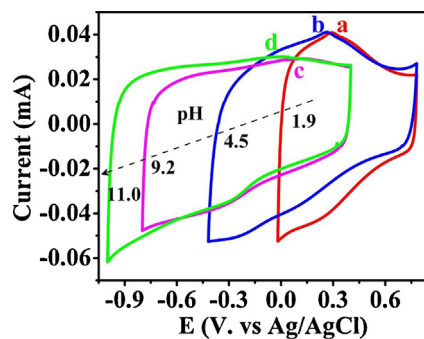


Fig. 4. CV curves of rGO in B-R buffer solution with pH 1.9 to 11.0 at the scan rate of 50 mV s^{-1} .

to 0.12 ($\text{Ag}/\text{Ag}_2\text{CO}_3$ -vis) after the formation of Ag NPs on Ag_2CO_3 and Ag_2CO_3 -GO-1.0 by photo-induced reduction, confirming the importance of the Ag SPR effect for enhancing the activity of the Ag_2CO_3 -based photocatalysts.

Furthermore, compared with pristine Ag_2CO_3 , all the photocatalysts based on Ag_2CO_3 with rGO or GO show the higher

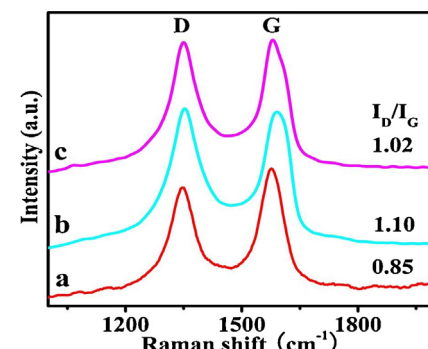


Fig. 6. Raman spectra of (a) GO, (b) rGO and (c) $\text{Ag}/\text{Ag}_2\text{CO}_3$ -rGO-1.0.

photocatalytic activities, which is ascribed to the effective transfer and separation of photogenerated charge carriers assisted by the graphitic structure of graphene. This result indicates the promoting effect of graphene as cocatalyst on the photocatalysis. Interestingly, rGO and GO as cocatalysts present the different promoting effect, and $\text{Ag}/\text{Ag}_2\text{CO}_3$ -rGO-1.0 shows higher activity than Ag_2CO_3 -

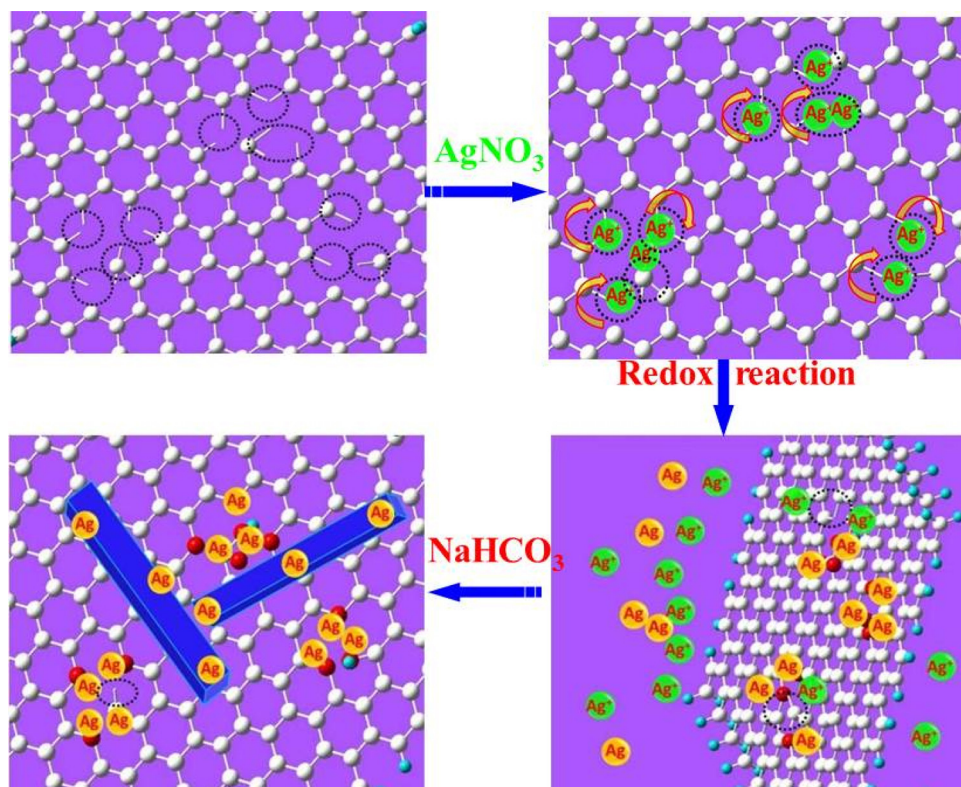


Fig. 5. The illustration of the synthesis mechanism for $\text{Ag}/\text{Ag}_2\text{CO}_3$ -rGO.

Table 2

Photocatalytic performance of each photocatalyst for the degradation of MO and phenol.

Sample	Irradiation time (min)/residue of MO (%)	k values of MO oxidation (min^{-1})	Irradiation time (min)/residue of phenol (%)	Rate constant (k) of phenol oxidation (min^{-1})
$\text{Ag}/\text{Ag}_2\text{CO}_3$ -rGO-0.5	30/13	0.08	/	/
$\text{Ag}/\text{Ag}_2\text{CO}_3$ -rGO-1.0	15/7	0.18	30/7	0.15
$\text{Ag}/\text{Ag}_2\text{CO}_3$ -rGO-1.5	25/10	0.11	/	/
$\text{Ag}/\text{Ag}_2\text{CO}_3$ -GO-vis	20/9	0.12	35/8	0.07
$\text{Ag}/\text{Ag}_2\text{CO}_3$ -vis	35/5	0.08	45/6	0.05
Ag_2CO_3 -GO-1.0	40/7	0.07	55/5	0.04
Ag_2CO_3	50/12	0.05	50/41	0.02
N-TiO_2	50/72	0.006	50/82	0.002

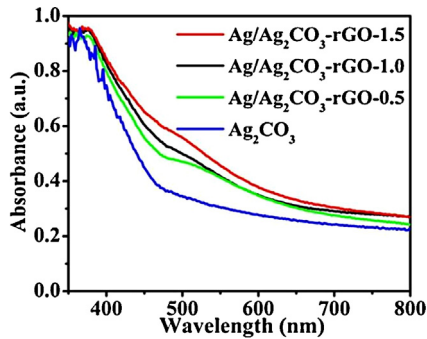


Fig. 7. UV-vis spectra of the Ag_2CO_3 and $\text{Ag}/\text{Ag}_2\text{CO}_3$ -rGO samples.

GO-1.0, which mainly arises from the spontaneous formation of plasmonic Ag with the participation of defects in rGO. The result indicates the structures of rGO show the more advantage than GO in adjusting Ag SPR and the photocatalytic activity. Meanwhile, the $\text{Ag}/\text{Ag}_2\text{CO}_3$ -rGO-1.0 presents the higher k value (0.18 min^{-1}) than $\text{Ag}/\text{Ag}_2\text{CO}_3$ -GO-vis (0.12 min^{-1}). It is observed that parts of Ag NPs

were located on rGO or even between the rGO sheets by the spontaneous redox reaction between the defects in rGO and Ag^+ ions (Fig. S2 in Supplementary materials). Thus, the formed Ag -rGO structures in $\text{Ag}/\text{Ag}_2\text{CO}_3$ -rGO-1.0 can increase the electrical conductivity compared with pristine GO film [64], which can efficiently promote the transfer and separation of photogenerated charge carriers. Therefore, the best photocatalytic activities for $\text{Ag}/\text{Ag}_2\text{CO}_3$ -rGO among all the prepared catalysts could be attributed to the synergistic effect of plasmonic Ag NPs and rGO, indicating the effect of defect structure and graphitic structure of rGO on the photocatalytic performance of $\text{Ag}/\text{Ag}_2\text{CO}_3$ -rGO.

The photocatalytic performance of the prepared photocatalysts was also evaluated by the photocatalytic oxidation of phenol aqueous solution under visible light irradiation, as shown in Fig. 9 and Table 2. From the residue content of phenol after irradiation and k value, the photocatalytic performances of these photocatalysts follow similar order: $\text{Ag}/\text{Ag}_2\text{CO}_3$ -rGO-1.0 > $\text{Ag}/\text{Ag}_2\text{CO}_3$ -GO-vis > $\text{Ag}/\text{Ag}_2\text{CO}_3$ -vis > Ag_2CO_3 -GO-1.0 > Ag_2CO_3 .

The good photocatalytic stability of catalysts is a fundamental requirement based on a high photocatalytic activity, and hence

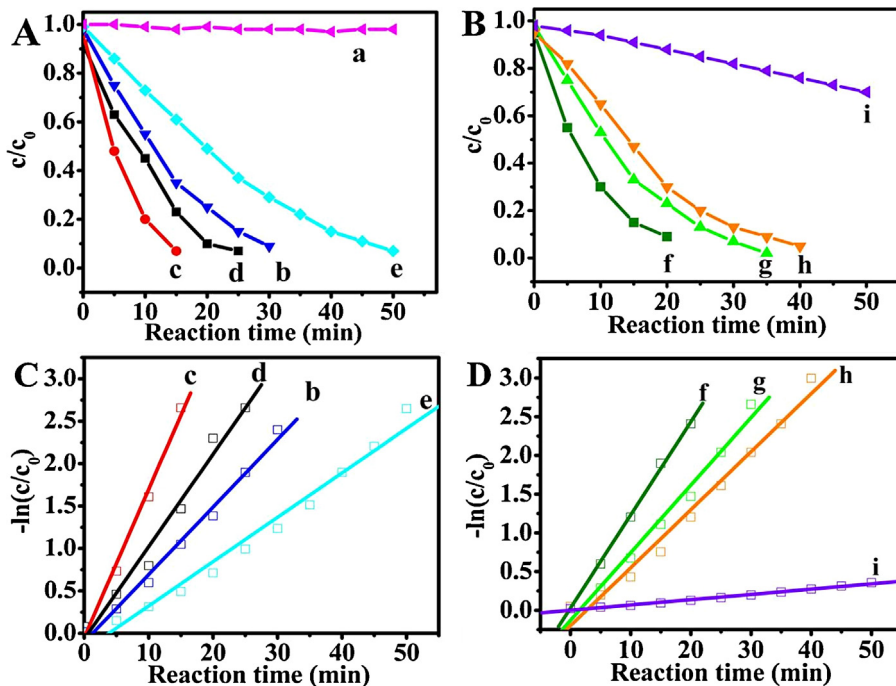


Fig. 8. The variation of MO concentration vs. illumination time (A,B) and the rate constant (k) of MO oxidation (C,D). (a) without photocatalyst, (b) $\text{Ag}/\text{Ag}_2\text{CO}_3$ -rGO-0.5, (c) $\text{Ag}/\text{Ag}_2\text{CO}_3$ -rGO-1.0, (d) $\text{Ag}/\text{Ag}_2\text{CO}_3$ -rGO-1.5, (e) Ag_2CO_3 , (f) $\text{Ag}/\text{Ag}_2\text{CO}_3$ -GO-vis, (g) $\text{Ag}/\text{Ag}_2\text{CO}_3$ -vis, (h) Ag_2CO_3 -GO-1.0 and (i) N-TiO_2 .

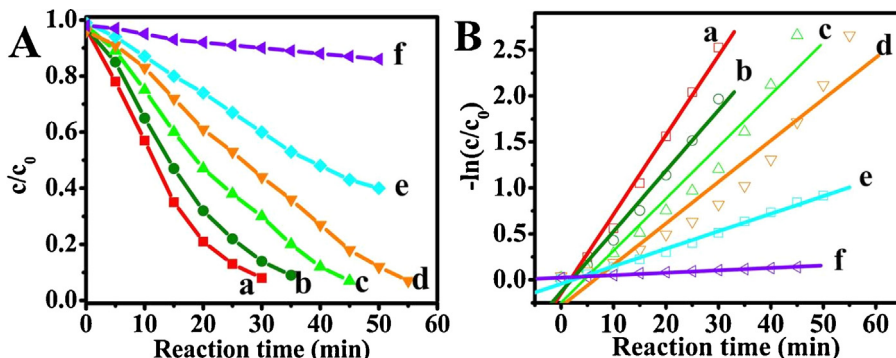


Fig. 9. The variation of phenol concentration vs. illumination time (A) and the rate constant (k) of phenol oxidation (B). (a) $\text{Ag}/\text{Ag}_2\text{CO}_3$ -rGO-1.0, (b) $\text{Ag}/\text{Ag}_2\text{CO}_3$ -GO-vis, (c) $\text{Ag}/\text{Ag}_2\text{CO}_3$ -vis, (d) Ag_2CO_3 -GO-1.0, (e) Ag_2CO_3 and (f) N-TiO_2 .

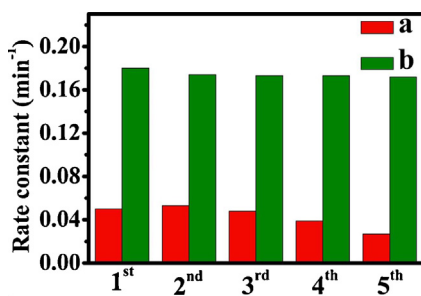


Fig. 10. Cycling runs in the photocatalytic oxidation of MO in the presence of Ag_2CO_3 (a) and $\text{Ag}/\text{Ag}_2\text{CO}_3\text{-rGO-1.0}$ (b).

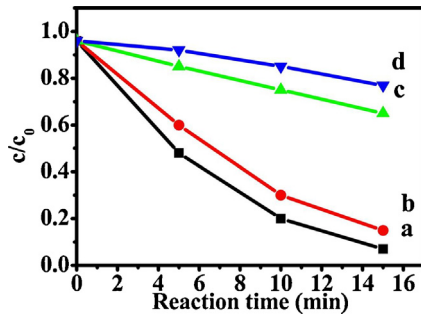


Fig. 11. Reactive species trapping experiments of $\text{Ag}/\text{Ag}_2\text{CO}_3\text{-rGO-1.0}$. (a) original reaction system without any scavenger, (b-d) adding BQ (b), TBA (c) and AO (d) scavengers.

the stability and recycle tests were investigated (Fig. 10). In the third cycle, Ag_2CO_3 almost lost their activity owing to the photocorrosion resulting from excessive Ag formed on the surface of Ag_2CO_3 . Notably, even after 5 successive cycles, $\text{Ag}/\text{Ag}_2\text{CO}_3\text{-rGO-1.0}$ still possesses the high activity for the photocatalytic oxidation of MO with a rate constant of reaction 0.171 min^{-1} (Fig. 10). This is ascribed to the effective transfer of photogenerated electrons by the graphitic structure of rGO, which greatly inhibits the photocorrosion to Ag_2CO_3 .

3.5. Photocatalytic mechanism for the $\text{Ag}/\text{Ag}_2\text{CO}_3\text{-rGO}$

To explore the essence of the high photocatalytic activity, trapping experiments of reactive oxygen species were developed and performed on $\text{Ag}/\text{Ag}_2\text{CO}_3\text{-rGO}$ photocatalysts (Fig. 11). Benzoquinone (BQ; a $\text{O}_2^{\bullet-}$ radical scavenger), ammonium oxalate (AO; a hole scavenger), and tert-butyl alcohol (TBA; a $\bullet\text{OH}$ scavenger) were used. The experimental results show that the addition of BQ in the reaction system had no obvious effect on the photodegradation process of MO, suggesting that $\text{O}_2^{\bullet-}$ is not the primary reactive species in the photocatalytic degradation process. When AO or TBA were used as scavenger, the photocatalytic activity of $\text{Ag}/\text{Ag}_2\text{CO}_3\text{-rGO-1.0}$ photocatalyst decreased from $\sim 100\%$ to 23% (AO) and 35% (TBA) in 15 min. Therefore, it is seen that hole and $\bullet\text{OH}$ are the primary reactive species in the photodegradation process of MO with using $\text{Ag}/\text{Ag}_2\text{CO}_3\text{-rGO}$ photocatalysts, which is further understood through the calculation of conduction band and valence band.

According to the Kubelka–Munk function [32,59,65], the indirect band-gap estimated from the onset of the curve edges is about 2.59 eV for the as-prepared Ag_2CO_3 sample. The valence band edge position of Ag_2CO_3 was estimated in this study according to the concepts of electro negativity, and the top of the VB and the bottom of the CB of Ag_2CO_3 were calculated to be 2.8 and 0.23 V (vs SHE). And both the CB potentials of Ag_2CO_3 and rGO are lower than that of $\text{O}_2/\text{H}_2\text{O}_2^-$ (-0.046 vs SHE), while higher than that of $\text{O}_2/\text{H}_2\text{O}_2$ (0.68 vs SHE). Therefore, hole and $\bullet\text{OH}$ are the primary reactive species

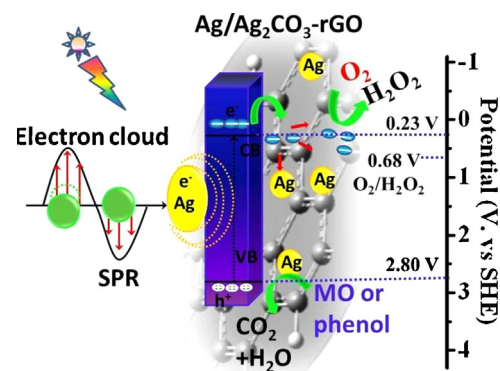


Fig. 12. The photocatalytic reaction and charge transfer mechanism of the $\text{Ag}/\text{Ag}_2\text{CO}_3\text{-rGO}$ photocatalyst under visible-light irradiation.

in the photodegradation process with using $\text{Ag}/\text{Ag}_2\text{CO}_3\text{-rGO}$ photocatalysts, which is consistent with the results of Fig. 11. Moreover, CB potential of Ag_2CO_3 is lower than the reduction potential of rGO, the photogenerated electron (e^-) in the CB of Ag_2CO_3 transfers to the surface of rGO, promoting the separation of photogenerated electron (e^-) and hole (h^+) for $\text{Ag}/\text{Ag}_2\text{CO}_3\text{-rGO}$. Furthermore, the plasmonic Ag NPs are very efficient at scattering and absorbing visible light, and the electrons of Ag NPs suffer a collective oscillation to yield SPR effect. The SPR results in the electric near-field on the Ag NP surface and all around Ag NPs. As displayed in Fig. 12, the electrons are transferred from the valence band to the conduction band of the Ag_2CO_3 under the visible light irradiation, thus, reducing recombination of electrons and holes. Therefore, $\text{Ag}/\text{Ag}_2\text{CO}_3\text{-rGO}$ photocatalysts show the high photocatalytic activities in the photocatalytic elimination of pollutants.

On the basis of the above experimental results, a possible mechanism is proposed to explain the significantly enhanced photocatalytic activity of the $\text{Ag}/\text{Ag}_2\text{CO}_3\text{-rGO}$ photocatalyst, as shown in Fig. 12. Due to the narrow band gap, Ag_2CO_3 can be easily excited to yield photogenerated electron-hole pairs under visible-light irradiation. Additionally, graphene with ultrahigh charge carrier mobility at room temperature, thus, can significantly enhance the transfer and separation of photogenerated electrons. This makes graphene to be an electron acceptor and electron transport “highway” in the composite photocatalytic system, which will suppress the recombination of photogenerated electron-hole pairs. As such, the photogenerated holes left behind in the VB of Ag_2CO_3 can directly oxidize MO or phenol to harmless products (e.g., CO_2 and H_2O). Simultaneously, the transferred photogenerated electrons on the surface of rGO can reduce the adsorbed O_2 to yield H_2O_2 , finally leading to the formation of $\bullet\text{OH}$, which is a powerful oxidative species for MO or phenol oxidation. Moreover, the formed Ag NPs can be excited by the visible light to generate a strong SPR effect due to the collective oscillation of the electrons on the metal surface, and SPR effect can induce an enhanced electric near-field at or around the metal and semiconductor interfaces. Thus, SPR effect can greatly promote the charge separation in Ag_2CO_3 and transfer the electron to rGO, which is beneficial to yielding more holes and $\bullet\text{OH}$ species to decompose pollutants.

4. Conclusion

Taking the advantage of the inherent chemical activity of rGO that arises from the defect structure introduction, we have developed a facile strategy for the construction of plasmonic $\text{Ag}/\text{Ag}_2\text{CO}_3\text{-rGO}$ photocatalysts. Compared with pristine Ag_2CO_3 and $\text{Ag}_2\text{CO}_3\text{-GO-1.0}$ photocatalysts, the constructed $\text{Ag}/\text{Ag}_2\text{CO}_3\text{-rGO}$ photocatalysts show much higher visible photocatalytic

activities and stabilities for the photocatalytic elimination of MO and phenol. The good performance of the catalysts mainly arises from the synergetic action of the electron-mediator effect of rGO and the SPR-enhanced charge separation of Ag. The present work can provide new insight for the design of high-performance photocatalytic materials.

Acknowledgments

This work was partially supported by the 973 program (2013CB632402), NSFC (51320105001, 51372190, 51402025, 21177100, and 21307011), Deanship of Scientific Research (DSR) of King Abdulaziz University (90-130-35-HiCi), Fundamental Research Funds for the Central Universities (WUT: 2014-VII-010), and Self-determined and Innovative Research Funds of SKLWUT (2013-ZD-1). This research is financially supported by the General Financial Grant from the China Postdoctoral Science Foundation (2014M562075 and 2015T80849).

References

- [1] M.R. Hoffmann, S.T. Martin, W. Choi, D.W. Bahnemann, *Chem. Rev.* 95 (1995) 69–96.
- [2] Q.J. Xiang, J.G. Yu, M. Jaroniec, *Chem. Soc. Rev.* 41 (2012) 782–796.
- [3] S.W. Cao, J.G. Yu, *J. Phys. Chem. Lett.* 5 (2014) 2101–2107.
- [4] J.G. Yu, J.X. Low, W. Xiao, P. Zhou, M. Jaroniec, *J. Am. Chem. Soc.* 136 (2014) 8839–8842.
- [5] Z.G. Zhao, M. Miyauchi, *Angew. Chem. Int. Ed.* 47 (2008) 7051–7055.
- [6] K. Nagaveni, M.S. Hegde, G. Madras, *J. Phys. Chem. B* 108 (2004) 20204–20212.
- [7] E. Thimsen, S. Biswas, C.S. Lo, P. Biswas, *J. Phys. Chem. C* 113 (2009) 2014–2021.
- [8] J. Choi, H. Park, M.R. Hoffmann, *J. Phys. Chem. C* 114 (2010) 783–792.
- [9] O. Sacco, V. Vaiano, C. Han, D. Sannino, D.D. Dionysiou, *Appl. Catal. B: Environ.* 164 (2015) 462–474.
- [10] H. Song, Y.G. Li, Z.R. Li, M. Xiao, L. Hu, Z.Z. Ye, L.P. Zhu, *Appl. Catal. B: Environ.* 166–167 (2015) 112–120.
- [11] R. Asahi, T. Morikawa, T. Ohwaji, K. Aoki, Y. Taga, *Science* 293 (2001) 269–271.
- [12] C.J. Huang, J.L. Hu, S. Cong, Z.G. Zhao, X.Q. Qiu, *Appl. Catal. B: Environ.* 174 (2015) 105–112.
- [13] J.L. Hu, W.J. Fan, W.Q. Ye, C.J. Huang, X.Q. Qiu, *Appl. Catal. B: Environ.* 158–159 (2014) 182–189.
- [14] M.C. Long, P.D. Hu, H.D. Wu, Y.Y. Chen, B.H. Tan, W.M. Cai, *J. Mater. Chem. A* 3 (2015) 5592–5598.
- [15] M.C. Long, Y.L. Qin, C. Chen, X.Y. Guo, B.H. Tan, W.M. Cai, *J. Phys. Chem. C* 117 (2013) 16734–16741.
- [16] G.H. Dong, W.K. Ho, L.Z. Zhang, *Appl. Catal. B: Environ.* 168–169 (2015) 490–496.
- [17] J. Zhang, J.G. Yu, M. Jaroniec, J.R. Gong, *Nano Lett.* 12 (2012) 4584–4589.
- [18] X. Zong, H.J. Yan, G.P. Wu, G.J. Ma, F.Y. Wen, L. Wang, C. Li, *J. Am. Chem. Soc.* 130 (2008) 7176–7177.
- [19] K. Chang, Z.W. Mei, T. Wang, S.X. Ouyang, J.H. Ye, *ACS Nano* 8 (2014) 7078–7087.
- [20] J. Zhang, L.F. Qi, J.R. Ran, J.G. Yu, S.Z. Qiao, *Adv. Energy Mater.* 4 (2014) 1301925.
- [21] C.H. Li, F. Wang, J. Zhu, J.C. Yu, *Appl. Catal. B: Environ.* 100 (2010) 433–439.
- [22] M. Antoniadou, V.M. Dascalaki, N. Balis, D.L. Kondratis, C. Kordulis, P. Lianos, *Appl. Catal. B: Environ.* 107 (2011) 188–191.
- [23] S.B. Wang, X.C. Wang, *Appl. Catal. B: Environ.* 162 (2015) 494–500.
- [24] J. Di, J.X. Xia, Y.P. Ge, H.P. Li, H.Y. Ji, H. Xu, Q. Zhang, H.M. Li, M.N. Li, *Appl. Catal. B: Environ.* 168–169 (2015) 51–61.
- [25] X. Zhao, T.G. Xu, W.Q. Yao, C. Zhang, Y.F. Zhu, *Appl. Catal. B: Environ.* 72 (2007) 92–97.
- [26] J.Z. Li, J.B. Zhong, X.Y. He, S.T. Huang, J. Zeng, J.J. He, W.L. Shi, *Appl. Surf. Sci.* 284 (2013) 527–532.
- [27] Y.N. Huo, X.F. Chen, J. Zhang, G.F. Pan, J.P. Jia, H.X. Li, *Appl. Catal. B: Environ.* 148–149 (2014) 550–556.
- [28] Y.P. Bi, S.X. Ouyang, N. Umezawa, N. Umezawa, J.Y. Cao, J.H. Ye, *J. Am. Chem. Soc.* 133 (2011) 6490–6492.
- [29] P. Wang, Y. Xia, P.P. Wu, X.F. Wang, H.G. Yu, J.G. Yu, *J. Phys. Chem. C* 118 (2014) 8891–8898.
- [30] H.G. Yu, G.Q. Cao, F. Chen, X.F. Wang, J.G. Yu, M. Lei, *Appl. Catal. B: Environ.* 160–161 (2014) 658–665.
- [31] Y. Maruyama, H. Irie, K. Hashimoto, *J. Phys. Chem. B* 110 (2006) 23274–23278.
- [32] X.X. Hu, C. Hu, J.H. Qu, *Mater. Res. Bull.* 43 (2008) 2986–2997.
- [33] G.P. Dai, J.G. Yu, G. Liu, *J. Phys. Chem. C* 116 (2012) 15519–15524.
- [34] M.C. Long, W.M. Cai, *Nanoscale* 6 (2014) 7730–7742.
- [35] C.J. Huang, W.Q. Ye, Q.W. Liu, X.Q. Qiu, *ACS Appl. Mater. Interfaces* 6 (2014) 14469–14476.
- [36] W.B. Sun, H.Y. Zhang, J. Lin, *J. Phys. Chem. C* 118 (2014) 17626–17632.
- [37] W.K. Ho, Z.Z. Zhang, W. Lin, S.P. Huang, X.W. Zhang, X.X. Wang, Y. Huang, *ACS Appl. Mater. Interfaces* 7 (2015) 5497–5505.
- [38] M.S. Wang, C.B. Gao, L. He, Q.P. Lu, J.Z. Zhang, C. Tang, S. Zorba, Y.D. Yin, *J. Am. Chem. Soc.* 135 (2013) 15302–15305.
- [39] C.H. An, S.N. Peng, Y.G. Sun, *Adv. Mater.* 22 (2010) 2570–2574.
- [40] P. Wang, B.B. Huang, Z.H. Lou, Z.Y. Zhang, X.Y. Qin, Y. Dai, Z.K. Zheng, X.N. Wang, *Chem. Eur. J.* 16 (2010) 538–544.
- [41] Z.K. Zheng, T. Tachikawa, T. Majima, *J. Am. Chem. Soc.* 136 (2014) 6870–6873.
- [42] Z.F. Bian, T. Tachikawa, P. Zhang, M. Fujitsuka, T. Majima, *J. Am. Chem. Soc.* 136 (2014) 458–465.
- [43] L.Q. Liu, S.X. Ouyang, J.H. Ye, *Angew. Chem. Int. Ed.* 52 (2013) 6689–6693.
- [44] M.A. El-Sayed, *Acc. Chem. Res.* 34 (2001) 257–264.
- [45] K.L. Kelly, E. Coronado, L.L. Zhao, G.C. Schatz, *J. Phys. Chem. B* 107 (2003) 668–677.
- [46] L. Brus, *Acc. Chem. Res.* 41 (2008) 1742–1749.
- [47] Q.J. Xiang, J.G. Yu, M. Jaroniec, *J. Am. Chem. Soc.* 134 (2012) 6575–6578.
- [48] W.G. Wang, J.G. Yu, Q.J. Xiang, B. Cheng, *Appl. Catal. B: Environ.* 119–120 (2012) 109–116.
- [49] H. Li, Z.B. Xia, J.Q. Chen, L. Lei, J.H. Xing, *Appl. Catal. B: Environ.* 168–169 (2015) 105–113.
- [50] R.C. Pawar, C.S. Lee, *Appl. Catal. B: Environ.* 144 (2014) 57–65.
- [51] P. Gao, J.C. Liu, D.D. Sun, W. Ng, J. Hazard. Mater. 250–251 (2013) 412–420.
- [52] S. Yousefzadeh, M. Faraji, Y.T. Nien, A.Z. Moshfegh, *Appl. Surf. Sci.* 320 (2014) 772–779.
- [53] G.Q. Luo, X.J. Jiang, M.J. Li, Q. Shen, L.M. Zhang, H.G. Yu, *ACS Appl. Mater. Interfaces* 5 (2013) 2161–2168.
- [54] M. Zhu, P. Chen, M. Liu, *Langmuir* 28 (2012) 3385–3390.
- [55] X. Quan, H. Zhang, X.F. Fan, S. Chen, H.T. Yu, *Environ. Sci. Technol.* 45 (2011) 5731–5736.
- [56] C. Cui, Y.P. Wang, D.Y. Liang, W. Cui, H.H. Hu, B.Q. Lu, S. Xu, X.Y. Li, C. Wang, Y. Yang, *Appl. Catal. B: Environ.* 158–159 (2014) 150–160.
- [57] G.D. Chen, M. Sun, Q. Wei, Y.F. Zhang, B.C. Zhu, B. Du, J. Hazard. Mater. 244–245 (2013) 86–93.
- [58] T.F. Yeh, J.M. Syu, C. Cheng, T.H. Chang, H. Teng, *Adv. Funct. Mater.* 20 (2010) 2255–2262.
- [59] T.F. Yeh, F.F. Chan, C.T. Hsieh, H. Teng, *J. Phys. Chem. C* 115 (2011) 22587–22597.
- [60] J.H. Chen, M.Y. Wang, B. Liu, Z. Fan, K.Z. Cui, Y.F. Kuang, *J. Phys. Chem. B* 110 (2006) 11775–11779.
- [61] D.F. Xu, B. Cheng, S.W. Cao, J.G. Yu, *Appl. Catal. B: Environ.* 164 (2015) 380–388.
- [62] X.F. Wang, S.F. Li, H.G. Yu, J.G. Yu, *J. Mol. Catal. A: Chem.* 334 (2011) 52–59.
- [63] B.F. Xin, L.Q. Jing, Z.Y. Ren, B.Q. Wang, H.G. Fu, *J. Phys. Chem. B* 109 (2005) 2805–2809.
- [64] R. Pasricha, S. Gupta, A.K. Srivastava, *Small* 5 (2009) 2253–2259.
- [65] C.L. Yu, C. Li, S. Kumar, K. Yang, R.C. Jin, *Adv. Mater.* 26 (2014) 892–898.